

Influence of interface-induced valley-Zeeman and spin-orbit couplings on transport in graphene-on-WSe₂ heterostructures

M. Zubair,^{1,*} P. Vasilopoulos,^{1,†} and M. Tahir^{2,‡}

¹*Department of Physics, Concordia University, 7141 Sherbrooke Ouest, Montreal, Quebec H4B 1R6, Canada*

²*Department of Physics, Colorado State University, Fort Collins, CO 80523, USA*

We investigate the electronic dispersion and transport properties of graphene/WSe₂ heterostructures in the presence of a proximity induced spin-orbit coupling (SOC) using a low-energy Hamiltonian, with different types of symmetry breaking terms, obtained from a four-band, first and second nearest-neighbour tight-binding (TB) one. The competition between different perturbation terms leads to inverted SOC bands. Further, we study the effect of symmetry breaking terms on ac and dc transport by evaluating the corresponding conductivities within linear response theory. The scattering-independent part of the valley-Hall conductivity, as a function of the Fermi energy E_F , is mostly negative in the ranges $-\lambda_R \leq E_F$ and $E_F \geq \lambda_R$ when the strength λ_R of the Rashba SOC increases except for a very narrow region around $E_F = 0$ in which it peaks sharply upward. The scattering-dependent diffusive conductivity increases linearly with electron density, is directly proportional to λ_R in the low- and high-density regimes, but weakens for $\lambda_R = 0$. We investigate the optical response in the presence of a SOC-tunable band gap for variable E_F . An interesting feature of this SOC tuning is that it can be used to switch on and off the Drude-type intraband response. Furthermore, the ac conductivity exhibits interband responses due to the Rashba SOC. We also show that the valley-Hall conductivity changes sign when E_F is comparable to λ_R and vanishes at higher values of E_F . It also exhibits a strong dependence on temperature and a considerable structure as a function of the frequency.

I. INTRODUCTION

Two-dimensional (2D) materials have become a hot topic in solid state physics, especially since the discovery of graphene, both theoretically and experimentally because of their prominent mechanical, optical, electrical and magnetic properties [1]. Recently graphene has attracted a lot of attention in the field of spintronics due to its large electronic mobility, low spin-orbit coupling (SOC), negligible hyperfine interaction and gate tunability [2]. For a clear example, it has been proven that graphene exhibits a very long spin relaxation length even at room temperature [3, 4]. Due to the weak SOC though, it is not a suitable candidate for the observation of important spin-dependent phenomena including the spin-Hall effect [5] and anomalous Hall effect [6].

To render graphene useful in spintronics, several experimental groups used different techniques to tailor the SOC strength in it through coupling with foreign atoms or materials [7–13], such as graphene hydrogenation [14, 15] or fluorination [16] as well as heavy adatom decoration [17, 18]. However, these approaches not only reduce the transport quality, but also make it difficult to reproduce [14, 15] and detect [16–18] the induced SOC. To overcome these difficulties, graphene is recently grown on different novel 2D materials, which are ideal candidates to induce SOC via proximity effects [19–25]. Hexagonal boron nitride (BN) has a weak SOC, and therefore, is not a suitable substrate for the proximity effect

[26]. The family of 2D transition metal dichalcogenides (TMDCs) are the next best candidates, which have large direct band gaps and giant intrinsic SOC [27, 28]. In this respect, graphene on TMDCs has been investigated for transport [29–31] as well as intriguing technological applications, including field-effect tunnelling transistors (FETTs), radio-frequency oscillators, and efficient phototransistors [32–38]. Also, the proximity-induced SOC in graphene/TMDCs heterostructures has recently been shown to depend [39, 40] on the twist angle between the lattice of graphene and that of the TMDC.

In addition, it has been found in room-temperature experimental studies of the spin-Hall effect that few-layer WS₂ induces a large SOC in graphene, about 17 meV [41] as compared to the very weak one in pristine graphene [42]. Also, it has been unambiguously demonstrated experimentally that a room-temperature spin-Hall effect in graphene is induced by MoS₂ proximity [43]. Moreover, when graphene is placed on a multilayer WS₂ substrate, an additional valley-Zeeman SOC, due to the broken sublattice symmetry, along with the Rashba SOC have been predicted theoretically and observed experimentally [25, 44–46]. This SOC induces a spin splitting of degenerate bands, with out-of-plane spin polarization at the K and K' points, and an opposite spin splitting in different valleys. Analogous to the Zeeman splitting, the SOC is termed valley-Zeeman because the effective Zeeman fields are valley-dependent. It is the dominant SOC in TMDCs and is also predicted to be induced in graphene on TMDCs [25, 44–46]. To our knowledge though, apart from some spin-transport studies [47] and two experimental magneto-transport studies [48], neither ac and dc scattering-dependent charge transport nor the simultaneous effect of valley-Zeeman and Rashba SOC have been

* muhammad.zubair@mail.concordia.ca

† p.vasilopoulos@concordia.ca

‡ tahir@colostate.edu

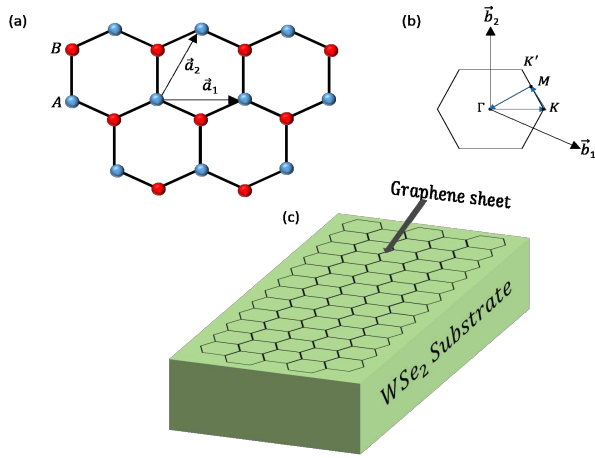


FIG. 1. (a) Real-space graphene with \vec{a}_1 and \vec{a}_2 the primitive lattice vectors. (b) Graphene's first Brillouin zone and high symmetry points Γ , K , and M in reciprocal space. Its primitive lattice vectors are \vec{b}_1 and \vec{b}_2 . (c) Schematic representation of graphene on a WSe_2 substrate.

theoretically studied in graphene on TMDCs.

In this work we study in detail the effect of the valley-Zeeman and Rashba-type SOC on ac and dc transport in graphene/ WSe_2 heterostructures. There results a mexican hat dispersion [49] contrary to other family members of TMDCs, e.g., MoS_2 , WS_2 etc. [50]. Such a dispersion leads to more features in the optical conductivity when the Fermi level moves between the minimum and maximum of the mexican hat. Also, we compare our results with those for pristine graphene.

In Sec. II we specify the Hamiltonian and obtain the eigenvalues and eigenfunctions in the presence of symmetry breaking terms. In Sec. III we present general expressions for the conductivities and provide numerical results. Conclusions and a summary follow in Sec. IV.

II. FORMULATION

Graphene is a 2D, one-atom thick planar sheet of bonded carbon atoms densely packed in a honeycomb structure as shown in Fig. 1 (a). The lattice structure can be viewed as a triangular lattice with two sites A (red filled spheres) and B (blue filled spheres) per unit cell. The arrows indicate the primitive lattice vectors $\vec{a}_1 = a(1, 0)$ and $\vec{a}_2 = a(1/2, \sqrt{3}/2)$, with a the triangular lattice constant of the structure, and span the graphene lattice. Further, \vec{a}_1 and \vec{a}_2 generate the reciprocal lattice vectors of the Brillouin zone, cf. Fig. 1 (b), given by $\vec{b}_1 = 4\pi/\sqrt{3}a(\sqrt{3}/2, -1/2)$ and $\vec{b}_2 = 4\pi/\sqrt{3}a(0, 1)$. From the explicit expressions of \vec{b}_1 and \vec{b}_2 we find the two inequivalent Dirac points (valleys) given by $\vec{K} = (4\pi/3a)(1, 0)$ and $\vec{K}' = (4\pi/3a)(1/2, \sqrt{3}/2)$.

The monolayer graphene system is described by the four-band, second nearest-neighbour tight-binding (TB)

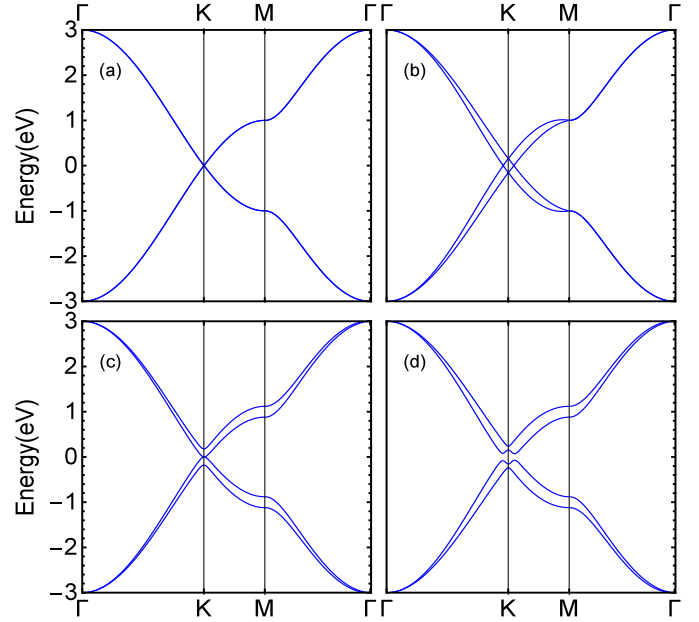


FIG. 2. Energy dispersion in a graphene/ WSe_2 heterostructure using the TB model (1) along the path $-M \rightarrow -K \rightarrow \Gamma \rightarrow K \rightarrow M \rightarrow \Gamma$ for (a) $\lambda_{c_i}, \lambda_R = 0$, (b) $\lambda_{c_i} \neq 0, \lambda_R = 0$, (c) $\lambda_{c_i} = 0, \lambda_R \neq 0$, and (d) $\lambda_{c_i}, \lambda_R \neq 0$.

Hamiltonian [23, 49, 51]

$$H = \sum_{\langle i,j \rangle, \alpha} t c_{i\alpha}^\dagger c_{j\alpha} + \sum_{i\alpha} \Delta \eta_{c_i} c_{i\alpha}^\dagger c_{i\alpha} + \sum_{\langle\langle i,j \rangle\rangle} \Delta_{ij} c_{i\alpha}^\dagger c_{j\alpha'} + \frac{2i}{3} \sum_{\langle i,j \rangle} \sum_{\alpha\alpha'} c_{i\alpha}^\dagger c_{j\alpha'} [\lambda_R (\mathbf{s} \times \hat{\mathbf{d}}_{ij})_z]_{\alpha\alpha'}. \quad (1)$$

Here $\Delta_{ij} = i\lambda_{c_i} \nu_{ij} s_z / 3\sqrt{3}$, $c_{i\alpha}^\dagger$ creates an electron with spin polarization α at site i that belongs to sublattice A or B , and $\langle i, j \rangle$ ($\langle\langle i, j \rangle\rangle$) runs over the nearest (second nearest) neighbouring sites. The second term is a staggered on-site potential, which takes into account the effective energy difference experienced by atoms at the lattice sites A ($\eta_{c_i} = +1$) and B ($\eta_{c_i} = -1$), respectively. The third and fourth terms represent the proximity-induced enhancement of the SOC due to a weak hybridization with the heavy atoms in WSe_2 . The third term is the valley-Zeeman SOC where $\nu_{ij} = +1$, if the second nearest hopping is anticlockwise with respect to the positive z axis, and $\nu_{ij} = -1$ if it is clockwise. The last term is the Rashba SOC parametrized by λ_R . It arises because the inversion symmetry is broken when the graphene sheet is placed on top of WSe_2 as shown in Fig. 1 (c). Also, $\hat{\mathbf{d}}_{ij} = \mathbf{d}_{ij}/|\mathbf{d}_{ij}|$, where $\mathbf{s} = (s_x, s_y, s_z)$ is the Pauli spin matrix and \mathbf{d}_{ij} the vector connecting the sites i and j in the same sublattice.

In Fig. 2 we plot the numerically evaluated energy dispersion of Eq. (1) to better understand the characteristics of the induced intrinsic SOC. Near the K point,

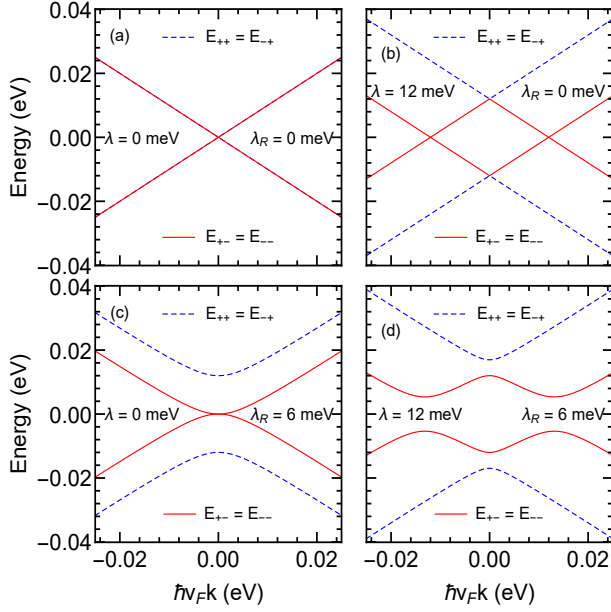


FIG. 3. Low-energy dispersion in a graphene/WSe₂ heterostructure for $\Delta = 0$ and different combinations of λ and λ_R .

for $\lambda_{c_i} = \lambda_R = 0$, the band structure has linear band crossings near $k = 0$ as can be seen from Fig. 2 (a). For $\lambda_{c_i} \neq 0$ and $\lambda_R = 0$ the spectrum is gapless and the spin degeneracy is broken away from $k = 0$, see Fig. 2 (b). Further, if only λ_R is present, the spectrum is also gapless, cf. Fig. 2 (c). However, a gap is created when both λ_{c_i} and λ_R are finite, cf. Fig. 2 (d).

We analyze the physics of electrons near the Fermi energy using a low-energy effective Hamiltonian derived from Eq. (1) and a Dirac theory around the K and K' valleys [23, 44, 46]. It reads

$$H_\eta^s = v_F(\eta\sigma_x p_x + \sigma_y p_y) + \Delta\sigma_z + \lambda\sigma_0 s\eta + \lambda_R(\eta s_y \sigma_x - s_x \sigma_y). \quad (2)$$

Here $\eta = \pm 1$ denotes the valleys K and K' , Δ is the mass term that breaks the inversion symmetry, $\lambda = \lambda_{c_i}$ is the valley-Zeeman SOC strength, λ_R the Rashba type SOC strength, $(\sigma_x, \sigma_y, \sigma_z)$ the Pauli matrix that corresponds to the pseudospin (i.e., $A - B$ sublattice), σ_0 is the unit matrix in the sublattice space, and v_F (8.2×10^5 m/s) denotes the Fermi velocity of Dirac fermions. For simplicity, we neglect the intrinsic SOC λ_i and consider only the $\lambda_R > \lambda_i$ case. Also, we expect that small but finite values of λ_i do not qualitatively affect our results as long as $\lambda \gg \lambda_i$. Further, we will also neglect the Δ term in our numerical treatment because $\lambda \gg \Delta$.

Upon diagonalizing Eq. (2) we obtain the dispersion

$$E_\xi(k) = l[\Delta^2 + \lambda^2 + \hbar^2 v_F^2 k^2 + 2\lambda_R^2 + 2s\sqrt{\Upsilon}]^{1/2}, \quad (3)$$

where $\Upsilon = \lambda_R^2(\lambda_R^2 - 2\lambda\Delta) + \hbar^2 v_F^2 k^2(\lambda_R^2 + \lambda^2) + \lambda^2 \Delta^2$ and $\xi = \{l, s\}$. Further, $l = +1(-1)$ denotes the conduction (valence) band and $s = +1(-1)$ represents the

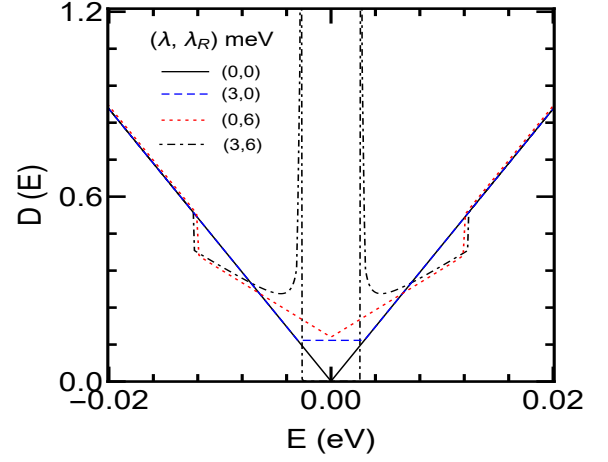


FIG. 4. Density of states for $(\lambda, \lambda_R) = (0, 0)$, $(\lambda, \lambda_R) = (3, 0)$ meV, $(\lambda, \lambda_R) = (0, 6)$ meV and $(\lambda, \lambda_R) = (3, 6)$ meV. All cases are for $\Delta = 0$.

spin-up (spin-down) branches. Notice that Eq. (3) has a valley degeneracy despite the valley-Zeeman term. The normalized eigenfunctions for both valleys are

$$\psi_\xi^+(k) = \frac{N_\xi^+}{\sqrt{S_0}} \begin{pmatrix} 1 \\ A_\xi^\eta e^{i\phi} \\ -iB_\xi^\eta e^{i\phi} \\ -iC_\xi^\eta e^{2i\phi} \end{pmatrix} e^{i\mathbf{k}\cdot\mathbf{r}}, \quad (4)$$

$$\psi_\xi^-(k) = \frac{N_\xi^-}{\sqrt{S_0}} \begin{pmatrix} -A_\xi^\eta e^{i\phi} \\ 1 \\ iC_\xi^\eta e^{2i\phi} \\ -iB_\xi^\eta e^{i\phi} \end{pmatrix} e^{i\mathbf{k}\cdot\mathbf{r}}, \quad (5)$$

respectively, with

$$N_\xi^\eta = l[1 + (A_\xi^\eta)^2 + (B_\xi^\eta)^2 + (C_\xi^\eta)^2]^{-1/2}, \quad (6)$$

$S_0 = L_x L_y$ the area of the sample, and $\phi = \tan^{-1}(k_y/k_x)$. Further, $A_\xi^\eta = (E_\xi^\eta - \eta\Delta - \eta\lambda)/\hbar v_F k$, $B_\xi^\eta = 2\lambda_R[(E_\xi^\eta)^2 - (\Delta + \lambda)^2]/\hbar v_F k[(E_\xi^\eta + \eta\lambda)^2 - \Delta^2 - \hbar^2 v_F^2 k^2]$, and $C_\xi^\eta = 2\lambda_R(E_\xi^\eta - \eta\Delta - \eta\lambda)/[(E_\xi^\eta + \eta\lambda)^2 - \Delta^2 - \hbar^2 v_F^2 k^2]$.

We plot Eq. (3) in Fig. 3 for different combinations of the λ and λ_R terms whose realistic values fall in the ranges 5 – 6 meV and 10 – 15 meV, respectively, as determined experimentally in Ref. 52. Here, the larger values of SOC are used just to see well-resolved bands splitting. For $\lambda = \lambda_R = 0$, the band structure has linear bands crossing near $k = 0$ for both valleys as can be seen from panel (a). For $\lambda \neq 0$ and $\lambda_R = 0$, the energy dispersion is spin non-degenerate and valley degenerate with a gapless behaviour as shown in panel (b). Further, the energy dispersion shows the gapless behaviour for $\lambda = 0$ and $\lambda_R \neq 0$ whereas it is spin-split as seen from panel (c). However, for λ and λ_R finite, the Rashba coupling

not only creates a gap between the conduction and valence band, by mixing the spin-up and spin-down states, but also produces an avoided crossing, see Fig. 1 (d). The analytical form of the momentum k_1 , at which an avoided crossing occurs, and of the gap $E_g = \Delta_1$ are

$$k_1 = \frac{1}{\hbar v_F} \left[\frac{(\lambda^2 + \lambda\Delta)(\lambda^2 + 2\lambda_R^2 - \lambda\Delta)}{\lambda^2 + \lambda_R^2} \right]^{1/2}, \quad (7)$$

$$\Delta_1 = 2\lambda_R \left[\frac{\lambda^2 + \Delta(2\lambda + \Delta)}{\lambda^2 + \lambda_R^2} \right]^{1/2}. \quad (8)$$

The density of states (DOS) per unit area corresponding to Eq. (3) is given by $D(E) = \sum_{\zeta} \delta(E - E_{\zeta})$ with $|\zeta\rangle = |\xi, \eta, k\rangle$. For $\lambda_R = 0$ it takes the simple form

$$D(E) = \frac{1}{2\pi\hbar^2 v_F^2} \sum_{\xi} \left| \frac{E}{l} - s\lambda \right| \Theta\left(\frac{E}{l} - s\lambda - \Delta\right), \quad (9)$$

and for $\Delta = \lambda = 0$ the form

$$D(E) = \frac{1}{2\pi\hbar^2 v_F^2} \sum_{\xi} \left| \frac{E}{l} - s\lambda_R \right| \Theta\left(\frac{E}{l} - (s+1)\lambda_R\right). \quad (10)$$

The DOS is shown in Fig. 4 for several values of λ and λ_R . The black curve is for monolayer graphene, with $\lambda = \lambda_R = 0$, and is included for comparison. The E_{+-} and E_{++} dispersions give rise to a square root singularity at $E = \lambda\lambda_R/\sqrt{\lambda^2 + \lambda_R^2}$ and a step at $E = \sqrt{\lambda^2 + 4\lambda_R^2}$, respectively, as shown by the black dot-dashed curve of Fig. 4. The origin of the singularity is the Mexican-hat energy dispersion, cf. Fig. 3. In addition, the step emerges from the bottom of the E_{++} band and is a van Hove singularity associated with the dispersion flattening at this point. The square root singularity is calculated near the Mexican-hat minimum $E = \lambda\lambda_R/\sqrt{\lambda^2 + \lambda_R^2}$ at which $D(E)$ reads

$$D(E) = \frac{k_1}{4\pi\hbar} \sqrt{\frac{2m^*}{E - \Delta_1}}, \quad (11)$$

with $m^* = \lambda_R(\lambda^2 + \lambda_R^2)^{3/2}/2v_F^2\lambda(\lambda^2 + 2\lambda_R^2)$ the effective mass and $E_{+,-} = \Delta_1 + (\hbar^2/2m^*)(k - k_1)^2$ the energy. This singularity is similar to that of the one-dimensional density of states. In the limit $\lambda_R = 0$ and $\lambda \neq 0$, the DOS has a finite value $\lambda/2\pi\hbar^2 v_F^2$ at $E = 0$ (see blue dashed curve). For $E \geq \lambda$, it increases linearly with E . Also, for $\lambda = 0$ and $\lambda_R \neq 0$, it is finite at $E = 0$ but has a step at $E = 2\lambda_R$, see the red dotted curve.

III. CONDUCTIVITIES

We consider a many-body system described by the Hamiltonian $H = H_0 + H_I - \mathbf{R} \cdot \mathbf{F}(t)$, where H_0 is the unperturbed part, H_I is a binary-type interaction (e.g., between electrons and impurities or phonons), and

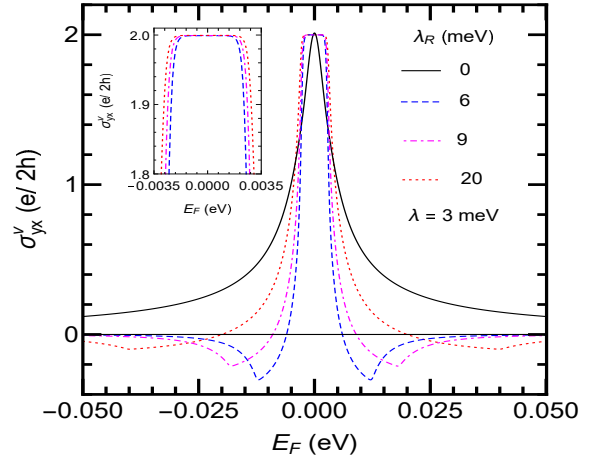


FIG. 5. Valley-Hall conductivity versus Fermi energy at $T = 0.5$ K. For further clarity, the range -0.35 meV $\leq E_F \leq 0.35$ meV is shown in the inset without the $\lambda_R = 0$ curve.

$-\mathbf{R} \cdot \mathbf{F}(t)$ is the interaction of the system with the external field $\mathbf{F}(t)$ [53]. For conductivity problems we have $\mathbf{F}(t) = e\mathbf{E}(t)$, where $\mathbf{E}(t)$ is the electric field, e the electron charge, $\mathbf{R} = \sum_i \mathbf{r}_i$, and \mathbf{r}_i the position operator of electron i . In the representation in which H_0 is diagonal the many-body density operator $\rho = \rho^d + \rho^{nd}$ has a diagonal part ρ^d and a nondiagonal part ρ^{nd} . For weak electric fields and weak scattering potentials, for which the first Born approximation applies, the conductivity tensor has a diagonal part $\sigma_{\mu\nu}^d$ and a nondiagonal part $\sigma_{\mu\nu}^{nd}$, the total conductivity is $\sigma_{\mu\nu}^T = \sigma_{\mu\nu}^d + \sigma_{\mu\nu}^{nd}$, $\mu, \nu = x, y$.

In general we have two kinds of currents, diffusive and hopping, with $\sigma_{\mu\nu}^d = \sigma_{\mu\nu}^{dif} + \sigma_{\mu\nu}^{col}$, but usually only one of them is present. If no magnetic field is present, the hopping term $\sigma_{\mu\nu}^{col}$ vanishes identically and only the term $\sigma_{\mu\nu}^{dif}$ survives. For elastic scattering it is given by [53]

$$\sigma_{\mu\nu}^d(\omega) = \frac{\beta e^2}{S_0} \sum_{\zeta} f_{\zeta}(1 - f_{\zeta}) \frac{v_{\nu\zeta} v_{\mu\zeta} \tau_{\zeta}}{1 + i\omega\tau_{\zeta}}, \quad (12)$$

with τ_{ζ} the momentum relaxation time, ω the frequency, and $v_{\mu\zeta}$ the diagonal matrix elements of the velocity operator. Further, $f_{\zeta} = [1 + \exp[\beta(E_{\zeta} - E_F)]]^{-1}$ is the Fermi-Dirac distribution function, $\beta = 1/k_B T$ and T the temperature.

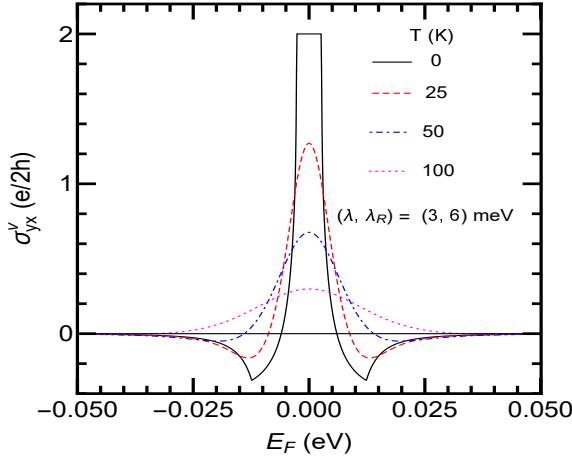
Regarding the contribution $\sigma_{\mu\nu}^{nd}$ one can use the identity $f_{\zeta}(1 - f_{\zeta'})[1 - \exp[\beta(E_{\zeta} - E_{\zeta'})]] = f_{\zeta} - f_{\zeta'}$, and cast the original form in the more familiar one [53]

$$\sigma_{\mu\nu}^{nd}(\omega) = \frac{i\hbar e^2}{S_0} \sum_{\zeta \neq \zeta'} \frac{(f_{\zeta} - f_{\zeta'}) v_{\nu\zeta'} v_{\mu\zeta'}}{(E_{\zeta} - E_{\zeta'})(E_{\zeta} - E_{\zeta'} + \hbar\omega - i\Gamma)}, \quad (13)$$

where the sum runs over all quantum numbers ζ and ζ' with $\zeta \neq \zeta'$. The infinitesimal quantity ϵ in the original form has been replaced by Γ_{ζ} to account for the broadening of the energy levels. In Eq. (13) $v_{\nu\zeta\zeta'}$ and $v_{\mu\zeta\zeta'}$ are the off-diagonal matrix elements of the

TABLE I. Band gap energies involved in optical transitions, cf. Fig. 7, for $\lambda = 8$ meV, $\lambda_R = 6$ meV, and two values of E_F .

Transition energies	Formula	$E_F = 6.6$ meV	$E_F = 9.6$ meV
Δ_1	$2\lambda\lambda_R/\sqrt{\lambda^2 + \lambda_R^2}$	9.6	9.6
Δ_2	$2\sqrt{(4\lambda^4 + 4\lambda_R^4 + 9\lambda^2\lambda_R^2)/(\lambda^2 + \lambda_R^2)}$	41.2	41.2
Δ_{01}	2λ	16	16
Δ_{02}	$2\sqrt{\lambda^2 + 4\lambda_R^2}$	28.8	28.8
Δ_a	$2\sqrt{2\lambda^2 + 2\lambda_R^2 + E_F^2 - 2M - 2L}$	32.2	
Δ_b	$2\sqrt{2\lambda^2 + 2\lambda_R^2 + E_F^2 + 2M + 2L}$	50	57.4

$$M = \sqrt{(\lambda^2 + \lambda_R^2)E_F^2 - \lambda^2\lambda_R^2}, \quad L = \sqrt{\lambda_R^4 + (\lambda^2 + \lambda_R^2)(E_F^2 + \lambda^2 \pm 2M)}$$
FIG. 6. Same as in Fig. 5 but for different values of T .

velocity operator. The relevant velocity operators are given by $v_x = \partial H/\hbar\partial k_x$ and $v_y = \partial H/\hbar\partial k_y$. With $\zeta = \{l, s, k, \eta\} = \{\xi, k, \eta\}$ for brevity, they read

$$\langle \zeta | v_x | \zeta' \rangle = v_F N_\xi^\eta N_{\xi'}^\eta (D_{\xi, \xi'}^\eta e^{i\phi} + F_{\xi, \xi'}^\eta e^{-i\phi}) \delta_{k, k'}, \quad (14)$$

$$\langle \zeta' | v_y | \zeta \rangle = i v_F N_\xi^\eta N_{\xi'}^\eta (D_{\xi, \xi'}^\eta e^{-i\phi} - F_{\xi, \xi'}^\eta e^{i\phi}) \delta_{k, k'}, \quad (15)$$

where $D_{\xi, \xi'}^\eta = A_{\xi'}^\eta + B_\xi^\eta C_{\xi'}^\eta$ and $F_{\xi, \xi'}^\eta = A_\xi^\eta + B_{\xi'}^\eta C_\xi^\eta$.

We now calculate the conductivity $\sigma_{yx}^{nd}(i\omega)$ given by Eq. (13). Further, the velocity matrix elements (14) and (15) are diagonal in k , therefore k will be suppressed in order to simplify the notation. The summation in Eq. (13) runs over all quantum numbers ξ, ξ', η, η' , and k . The parameter $\Gamma_{\eta\eta'}^{\xi\xi'}$, that takes into account the level broadening, is assumed to be independent of the band and valley indices, i.e., $\Gamma_{\eta\eta'}^{\xi\xi'} = \Gamma$. Using Eqs. (14) and

(15) we can express Eq. (13) as

$$\sigma_{yx}^{nd}(i\omega) = \frac{e^2 \hbar^2 v_F^2}{h} \sum_{\xi\xi'} \int dk k \frac{(N_\xi^\eta N_{\xi'}^\eta)^2 (f_{\xi k}^\eta - f_{\xi' k}^\eta)}{\Delta_{\xi\xi'}^\eta [(\Delta_{\xi\xi'}^\eta + \hbar\omega)^2 + \Gamma^2]} \times [\Delta_{\xi\xi'}^\eta + \hbar\omega - i\Gamma] [D_{\xi, \xi'}^\eta]^2 - (F_{\xi, \xi'}^\eta)^2] \quad (16)$$

where $\Delta_{\xi\xi'}^\eta = E_{\xi k}^\eta - E_{\xi' k}^\eta$. Further, in the limit $\Gamma = \omega = 0$, Eq. (16) reduces to

$$\sigma_{yx}^{nd} = \frac{e^2 \hbar^2 v_F^2}{h} \sum_{\xi\xi'} \int dk k \frac{(N_\xi^\eta N_{\xi'}^\eta)^2 (f_{\xi k}^\eta - f_{\xi' k}^\eta)}{(\Delta_{\xi\xi'}^\eta)^2} \times [(D_{\xi, \xi'}^\eta)^2 - (F_{\xi, \xi'}^\eta)^2] \quad (17)$$

In the valley-Hall effect electrons from regions near the inequivalent K and K' valleys flow to opposite transverse edges of the system, in the presence of SOCs when a longitudinal electric field is applied [54, 55]. The valley-Hall conductivity corresponding to Eq. (16) is defined by

$$\sigma_{yx}^v = \sum_{ss'} \sigma_{yx}^{nd}(\eta = +, s, s') - \sigma_{yx}^{nd}(\eta = -, s, s'). \quad (18)$$

The spin-Hall conductivity σ_{yx}^s , corresponding to Eq. (16), is finite only when both the Kane-Mele and valley-Zeeman SOCs are present. Hence, even in the presence of Rashba SOC, σ_{yx}^s vanishes [43]. Since a spin current is defined by $\mathbf{J}_s = (\hbar/2\mathbf{e})(\mathbf{J}_\uparrow - \mathbf{J}_\downarrow)$, we have to multiply σ_{yx}^v by $1/2e$ [5, 56]. Further, we find that charge Hall conductivity always vanishes

$$\sigma_{yx}^c = \sum_{\eta ss'} \sigma_{yx}^{nd}(\eta, s, s') = 0 \quad (19)$$

The component $\sigma_{xx}^{nd}(i\omega)$ is also obtained from Eq. (13):

$$\sigma_{xx}^{nd}(i\omega) = \frac{ie^2 \hbar^2 v_F^2}{h} \sum_{\eta\xi\xi'} \int dk k \frac{(N_\xi^\eta N_{\xi'}^\eta)^2 (f_{\xi k}^\eta - f_{\xi' k}^\eta)}{\Delta_{\xi\xi'}^\eta [(\Delta_{\xi\xi'}^\eta + \hbar\omega)^2 + \Gamma^2]} \times [\Delta_{\xi\xi'}^\eta + \hbar\omega - i\Gamma] [D_{\xi, \xi'}^\eta]^2 + (F_{\xi, \xi'}^\eta)^2]. \quad (20)$$

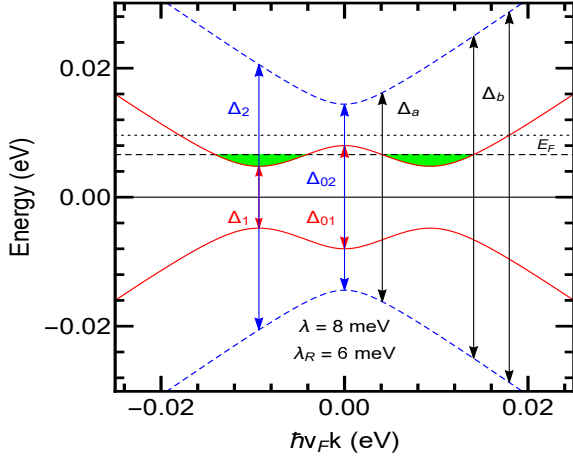


FIG. 7. Band structure near the Fermi energy E_F in the presence of SOC terms for $\lambda = 8$ meV and $\lambda_R = 6$ meV. The black dashed and dotted lines show $E_F = 6.6$ meV and $E_F = 9.6$ meV. The various gap energies, indicated by Δ_1 , Δ_2 , etc. are displayed in table I. Notice that for $E_F = 9.6$ meV the energy Δ_a does not contribute to any transitions.

For $\lambda = 0$ and $\lambda_R \neq 0$, Eq. (16) vanishes because the factor $(D_{\xi, \xi'}^\eta)^2 - (F_{\xi, \xi'}^\eta)^2$ becomes zero, whereas Eq. (20) survives. Moreover, in the limit $\lambda = \lambda_R = 0$, Eq. (20) reduces to the optical conductivity of pristine graphene, which is independent of $\hbar\omega$ and given by $e^2/2h$ [57].

We now consider the diagonal component σ_{xx}^d given by Eq. (12). Using Eq. (14), with $\xi = \xi'$, we obtain

$$\sigma_{xx}^d(i\omega) = \frac{e^2 v_F^2 \beta}{\pi} \sum_{\eta\xi} \int dk k (N_\xi^\eta)^4 f_{\xi k}^\eta (1 - f_{\xi k}^\eta) \times \frac{(A_\xi^\eta + B_\xi^\eta C_\xi^\eta)^2 \tau_{\xi k}^\eta}{1 + i\omega \tau_{\xi k}^\eta} \quad (21)$$

At very low temperatures we can make the approximation $\beta f_{\xi k}^\eta (1 - f_{\xi k}^\eta) \approx \delta(E_\xi - E_F)$ and $\tau_{\xi k}^\eta = \tau_{\xi k_F}^\eta$ because all states until the Fermi level are occupied.

In Fig. 5 we plot Eq. (16) in the dc limit ($\omega = 0$) as a function of E_F for $\Gamma = 0.2$ meV, $\lambda = 3$ meV and for different values of λ_R . When E_F is in the gap, i.e., in the range $-\lambda\lambda_R/\sqrt{\lambda^2 + \lambda_R^2} \leq E_F \leq \lambda\lambda_R/\sqrt{\lambda^2 + \lambda_R^2}$, the valley-Hall conductivity is quantized in units of $2e/2h$ similar to the case of gapped graphene and topological insulators [54, 58]. The reason is that the factor $\sum_{\eta\xi\xi'} (N_\xi^\eta N_{\xi'}^\eta)^2 [(D_{\xi, \xi'}^\eta)^2 - (F_{\xi, \xi'}^\eta)^2] / (\Delta_{\xi\xi'}^\eta)^2$, called Berry curvature $\Omega(k)$, of Eq. (16) in the limit $\omega = 0$ has a peak, which is well covered by occupied states for $E_F > \lambda\lambda_R/\sqrt{\lambda^2 + \lambda_R^2}$. As a consequence, the valley-Hall conductivity approaches the quantized value. For $\lambda\lambda_R/\sqrt{\lambda^2 + \lambda_R^2} \leq E_F \leq \lambda_R$, σ_{yx}^v decreases with E_F . Further, as can be seen, when E_F becomes comparable to λ_R , a sign change occurs in the conductivity which later vanishes at higher values of E_F , $E_F \gg \sqrt{\lambda^2 + 4\lambda_R^2}$. The change in sign is due to the Rashba coupling between the spin-up and spin-down bands. Furthermore,

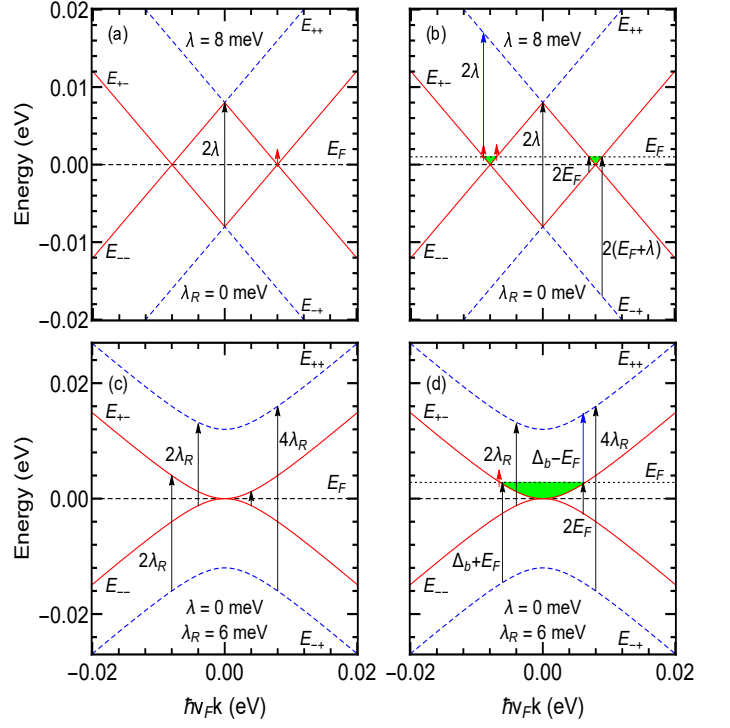


FIG. 8. Band structure near the Fermi energy E_F in the presence of SOC terms for $\lambda = 8$ meV and $\lambda_R = 6$ meV. Black and red arrows represent possible interband transitions. Red arrows indicate the Drude type intraband transitions. (a) $\lambda \neq 0$, $\lambda_R = 0$, $E_F = 0$. (b) $\lambda \neq 0$, $\lambda_R = 0$, $E_F = 1$ meV. (c) $\lambda_R \neq 0$, $\lambda = 0$, $E_F = 0$. (d) $\lambda_R \neq 0$, $\lambda = 0$, $E_F = 2.8$ meV.

this off-diagonal term in spin space permits transitions between two conduction spin subbands (see Eq. (3)), that could be interpreted as spin-flip transitions near the band touching. In addition, the coupling strength between opposite spin bands becomes weaker as λ_R increases. As a result, the negative part of the conductivity due to the spin-up band diminishes and σ_{yx}^v shows the usual behaviour of gapped graphene and topological insulators [54, 58]. Further, as can be seen in the inset, the band gap increases with λ_R . Also, the value of the conductivity at $E_F = 0$ is due to the finite one of Γ ($= 0.2$ meV); if we take $\Gamma = 0$, the conductivity diverges at $E_F = 0$ but its overall qualitative behavior remains as shown.

We now take into account the effect of temperature T on the valley-Hall conductivity contained in the Fermi function, which is independent of electron-phonon interaction in the first Born approximation [53]. The valley-Hall conductivity is evaluated numerically with the help of Eq. (16) and plotted in Fig. 6 for four values of T . We find a strong T dependence, particularly when the Fermi level is in the gap. The quantization of the valley-Hall conductivity is destroyed at high values of T . This occurs when the thermal broadening $k_B T$ becomes comparable to the energy gap. Notice that the effect of temperature on σ_{yx}^v is similar to that on the spin-Hall conductivity.

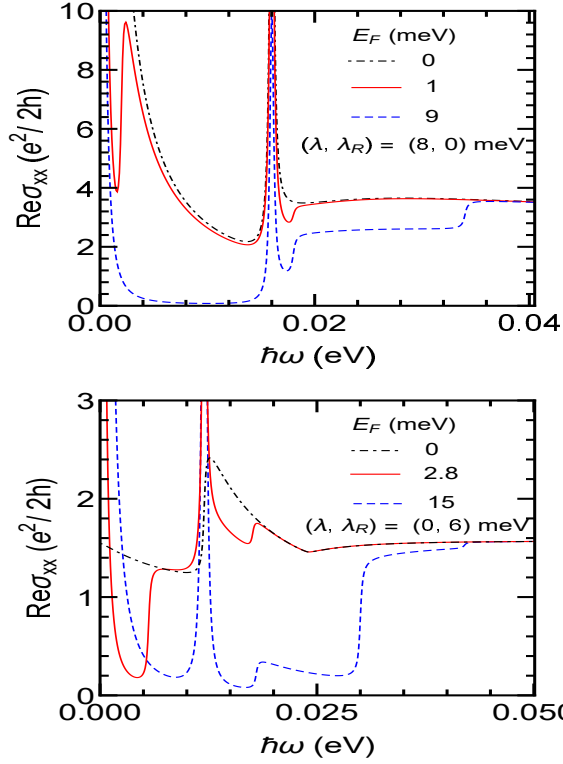


FIG. 9. Real part of longitudinal conductivity versus photon energy at $T = 0.5$ K. The upper panel is for $\lambda_R = 0$ and the lower one is for $\lambda_R \neq 0$.

ity in a graphene/MoS₂ heterostructure by considering valley-Zeeman and Kane-Mele SOC in the absence of the Rashba SOC.

Various transition energies, which play an important role in the optical conductivity, are shown in Fig. 7 for $\lambda, \lambda_R \neq 0$. Their analytical expressions are displayed in table I. Notice that for $E_F = 6.6$ meV, the energies Δ_a and Δ_b , indicated with black arrows, become also important in optical transitions, since E_F crosses the curve E_{+-} at two values of the momentum. However, for $E_F = 9.6$ meV, only Δ_b contributes to optical transitions because E_F cuts E_{+-} curve only at one value of the momentum. In Fig. 8, we show possible allowed interband and intraband transitions by contrasting the case $\lambda \neq 0, \lambda_R = 0$ in the upper panels and the case $\lambda = 0, \lambda_R \neq 0$ in the lower panels. The blue arrows represent the interband transitions $E_{+-} \rightarrow E_{++}$ for $0 < E_F < \lambda$ and $0 < E_F < \lambda_R$ as can be seen in Fig. 8 (b) and (d). The black arrows represent the allowed interband transitions $E_{-+} \rightarrow E_{+-}(E_{++})$ and $E_{--} \rightarrow E_{+-}(E_{++})$ for $E_F = 0$ and $E_F \neq 0$, respectively, while the red arrows indicate intraband transitions that occur near E_F .

Now we present results for the real part of Eqs. (20) and (21) ($\text{Re}\sigma_{xx} = \text{Re}\sigma_{xx}^d + \text{Re}\sigma_{xx}^{nd}$), evaluated numerically, versus $\hbar\omega$ using a Lorentzian form of Dirac delta function and taking $\Gamma = 0.2$ meV for $T \neq 0$. We start from the upper panel of Fig. 9 by considering

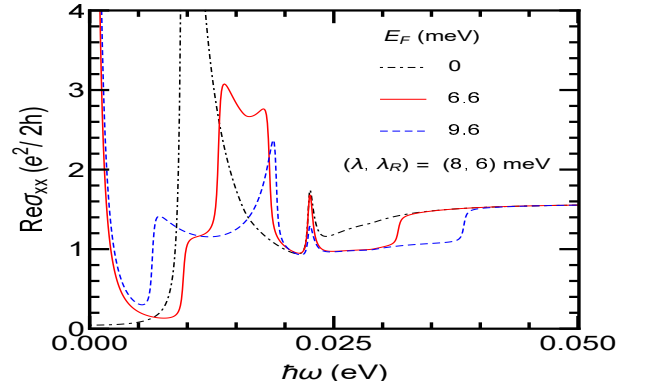


FIG. 10. Same as in Fig. 9 but for $\lambda, \lambda_R \neq 0$.

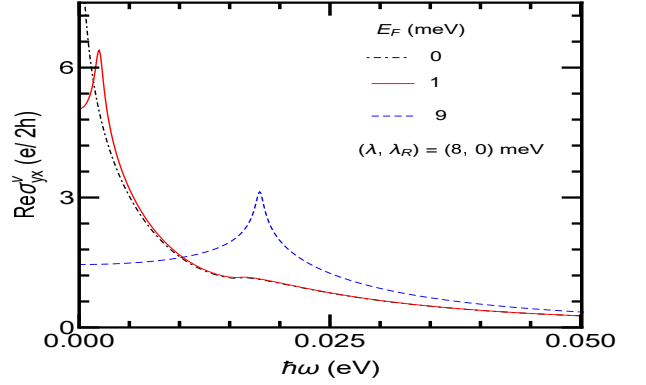


FIG. 11. Valley-Hall conductivity versus photon energy for $\lambda_R = 0$ at $T = 0.5$ K.

the case $\lambda \neq 0$ and $\lambda_R = 0$. The transitions are vertical for photon's momentum $q \sim 0$ and connect the filled valence band to empty conduction band, see Fig. 8 (a). For the case of $E_F = 0$, intraband response appears due to the transition $E_{+-} \rightarrow E_{+-}$ and has a δ function form, centred around $\hbar\omega = 0$, which broadens the peak when any kind of scattering is taken into account. Further, intraband responses occur when the Fermi level is located away from the Dirac point. For $\hbar\omega = 2\lambda$ we obtain another Dirac delta peak due to the transition from $E_{--} \rightarrow E_{+-}$, which is also broadened through $i\pi\delta(x) = \lim_{\Gamma \rightarrow 0} (1/x - i\Gamma)$, cf. Eq. (20). For $0 < E_F < \lambda$, the new absorption peaks appear at $\hbar\omega = 2E_F$ and $\hbar\omega = 2(E_F + \lambda)$ due to the possible transitions $E_{--} \rightarrow E_{+-}$ and $E_{-+} \rightarrow E_{+-}$. For $E_F > \lambda$, the absorption peaks disappear below $\hbar\omega < 2\lambda$ because the transition $E_{--} \rightarrow E_{+-}$ is no longer possible due to the filling of states below the Fermi level that are Pauli blocked. Further, the Drude peak persists at low $\hbar\omega$, but now two other pieces of interband transitions emerge with onsets at $\Delta_a + E_F$ and $\Delta_b + E_F$.

In the lower panel of Fig. 9 we show the results for real part of the longitudinal conductivity for $\lambda = 0, \lambda_R \neq 0$ for different values of E_F . For $E_F = 0$, we can see that there is a peak at $2\lambda_R$ which is the separation between

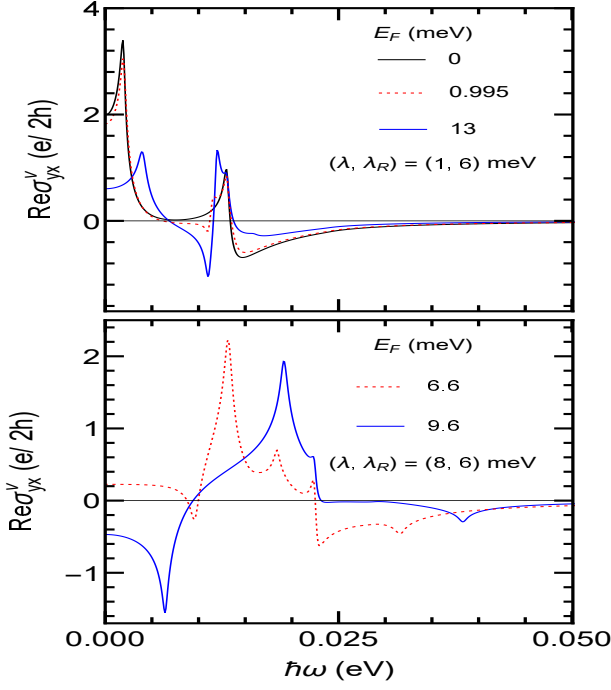


FIG. 12. Same as in Fig. 11 but with the upper panel for $\lambda_R > \lambda$ and the lower one for $\lambda_R < \lambda$.

E_{--} and E_{+-} bands. In addition, there is a kink at $4\lambda_R$ due to the transition $E_{-+} \rightarrow E_{++}$. As we increase the Fermi level, say, $0 < E_F < \lambda_R$ and $E_F > \lambda_R$, the peak becomes sharper and we see an onset of a Drude contribution at low $\hbar\omega$ due to intraband transitions $E_{+-} \rightarrow E_{+-}$ and $E_{++} \rightarrow E_{++}$ in contrast to $E_F = 0$ case (black dot-dashed curve). Further, for finite values of E_F , we see the steps at $2E_F$ similar to monolayer graphene ($\lambda = \lambda_R = 0$) as well as features at $\Delta_a + E_F$, $\Delta_b - E_F$, and $\Delta_b + E_F$ above which we attain the flat absorption like pristine graphene [57]. Note that our results are similar to bilayer graphene [59, 60]. But here, the Rashba SOC, which allows the interband transitions between opposite spin bands, gives rise to the absorption peaks, while these peaks in bilayer graphene are due to interlayer hopping between two graphene sheets.

The real part of the longitudinal conductivity as a function of the photon energy, for $\lambda, \lambda_R \neq 0$, is shown in Fig. 10 for several values of E_F : (i) just below the maximum of the Mexican hat i.e. $\lambda\lambda_R/(\lambda^2 + \lambda_R^2)^{1/2} < E_F < \lambda$ (ii) just above the Mexican hat, i.e., for $\lambda < E_F < (\lambda^2 + 2\lambda_R^2)^{1/2}$. For $E_F = 0$ we find a large absorption peak at approximately $2\lambda_R$, which corresponds to transitions between the two square-root singularities of the DOS, see Fig. 4, or transitions between the two minima of the Mexican hat structures of the E_{--} and E_{-+} bands. As E_F moves into the Mexican hat, this feature disappears because states below E_F are occupied and, therefore, Pauli blocked. Further, the major peaks are due to the transitions $E_{+-} \rightarrow E_{++}$, $E_{--} \rightarrow E_{-+}$, $E_{--} \rightarrow E_{++}$ and $E_{-+} \rightarrow E_{++}$, respectively. The gap energies which

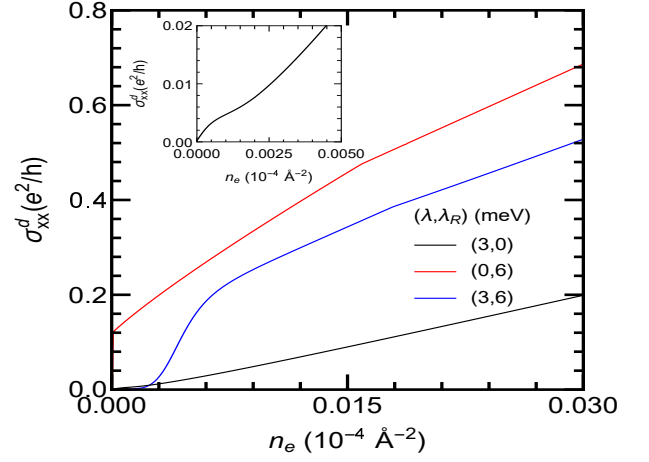


FIG. 13. Longitudinal conductivity σ_{xx}^d in units of e^2/h versus electron concentration n_e for different values of λ and λ_R . For further clarity, the range 0–5 meV is shown in inset.

contribute to the onset of these transition peaks are indicated in Fig. 7 and given analytically in table I. Also, the conductivity retains the flat absorption at sufficiently higher values of $\hbar\omega$ similar to pristine graphene [57].

Plots of the real part of σ_{yx}^v for $E_F = 0$ (black dot-dashed curve) and $E_F \neq 0$ (red and blue dashed curves) in the absence of Rashba SOC ($\lambda_R = 0$) are shown in Fig. 11. In the dc limit, the expected value of the valley-Hall conductivity is obtained as can be seen in Fig. 5 (black curve). If the system is illuminated by photons of frequency ω , the amplitude of the absorption peaks is suppressed for $E_F = 0$, while an increase in it is observed for $E_F \neq 0$. For $\hbar\omega = 2|\lambda|$ a strong valley-Hall response is observed for $E_F \neq 0$. Therefore, it can be expected that a stronger valley-Hall response may be accessible when the photon energy is tuned to the valley-Zeeman SOC. For $\hbar\omega > 2|\lambda|$, σ_{yx}^v decreases rapidly and approaches zero at sufficiently higher values of $\hbar\omega$.

The real part of the valley-Hall conductivity is shown in Fig. 12 for several values of E_F . In the dc limit ($\omega = 0$), we obtain the quantized value of the valley-Hall conductivity ($\text{Re}\sigma_{yx}^v = e/h$) for $E_F = 0$ (black curve in the upper panel). If the system is subjected to a photon of frequency ω , an increase in the magnitude of the valley-Hall response is observed. The absorption peaks occur at the same onset energies as indicated in Fig. 7. For example, the first peak appeared when $\hbar\omega = 2\Delta_1$ or transition between the minima of the E_{--} and E_{+-} bands. Further, the change in sign of the conductivity is due to the Rashba SOC, which is responsible for the coupling between spin-up and spin-down bands e.g., the transition from the maximum of Mexican hat of E_{--} band to the minimum of E_{++} band around $k = 0$. Furthermore, for finite values of E_F we obtain new features in the optical spectrum due to the emergence of new transitions such as $E_{+-} \rightarrow E_{++}$, e.g., some features are completely removed due to Pauli blocking. Also, the valley-Hall response is diminished at sufficiently high frequencies. However, in

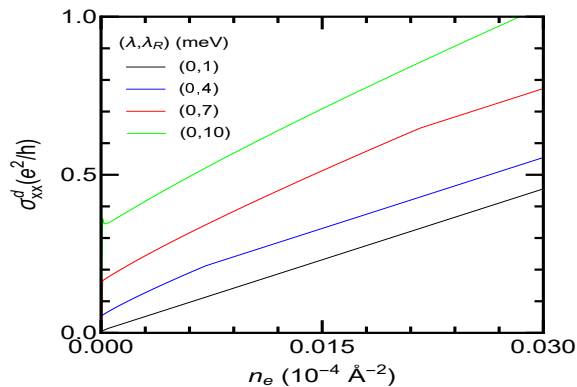


FIG. 14. Same as in Fig. 13 but for different values of λ_R .

the case of $\lambda_R < \lambda$ (lower panel), the difference among the optical transition energies is significantly enhanced due to larger values of λ and new features emerge at the momenta at which E_F crosses the E_{+-} band (see Fig. 7). Moreover, some of the optical transitions are no longer possible, e.g., $E_{--} \rightarrow E_{+-}$ when E_F is just above the mexican hat because the states below it are occupied and, therefore, Pauli blocked (blue curve).

In Fig. 13 we plot σ_{xx}^d , from Eq. (21), by evaluating it numerically versus electron concentration (n_e) and using the expression of τ given in Appendix A but evaluated at the Fermi level, $k = k_F$. The conductivity increases with E_F and therefore with the carrier density n_e . The diffusive conductivity increases linearly with n_e but cusp-like features appear when E_{++} band begin to occupied at specific values of n_e in contrast to pristine graphene [61, 62]. This behaviour makes graphene/WS₂ a suitable candidate for charge switches contrary to pristine graphene. The screening effect becomes significantly weaker when only the λ term is present. Moreover, the conductivity shown in Fig. 14 increases in the low-density regime for $\lambda = 0$ and $\lambda_R \neq 0$ as compared to the $\lambda \neq 0$, $\lambda_R = 0$ and $\lambda, \lambda_R \neq 0$ case. In the limit $\lambda = \lambda_R = 0$ we obtain the result similar to pristine graphene [61, 62].

IV. SUMMARY AND CONCLUSION

We studied the energy dispersion of graphene/WSe₂ heterostructures by using a TB model in the presence

of valley-Zeeman and Rashba SOCs. We found that the effective Hamiltonian (2) derived from the TB one (1) nicely captures the low-energy physics near the K and K' valleys. We demonstrated that the density of states has a finite value around $E = 0$ in both cases $\lambda \neq 0$, $\lambda_R = 0$ and $\lambda = 0$, $\lambda_R \neq 0$. In addition, it has a square root singularity when both λ and λ_R are present. This singularity is similar to that in biased bilayer graphene; however, here it is due to the Rashba SOC whereas in biased bilayer graphene it is due to interlayer hopping. We also found that the ac and dc valley-Hall conductivities change sign in the presence of the λ_R term, which leads to interband transitions. Also, the band gap is enhanced by increasing the strength λ_R . Further, for $\lambda_R \gg \lambda$ the valley-Hall conductivity exhibits a behaviour similar to that in gapped graphene and topological insulators [54, 58]. The screening effect in the diffusive conductivity is dominant only when the Rashba SOC is present, whereas it is significantly suppressed for $\lambda \neq 0$, $\lambda_R = 0$. Also, the conductivity increases with λ_R in the low- and high-density regimes, see Fig. 14.

The dc valley-Hall conductivity changes sign when E_F is comparable to λ_R and vanishes at higher values of E_F , cf. Fig. 5. It also exhibits a strong temperature dependence when the Fermi level in the gap, cf. Fig. 6.

The intraband response of the ac longitudinal conductivity for $\lambda_R = 0$ (see upper panel of Fig. 9) shifts towards lower photon energies when E_F increases compared to $\lambda_R \neq 0$ (see lower panel of Fig. 9 and Fig. 10). We also noted the switching on and off of the Drude response when the Fermi energy is varied (see Fig. 10), which may be of interest in technological applications. In addition, for $\lambda, \lambda_R \neq 0$ new onsets in the optical conductivity appear due to the shifting of the Fermi level through the mexican hat structure (see Figs. 10 and 12), which may be a promising feature in optical experiments. Our findings may be pertinent to developing future spintronics and valleytronics devices such as field-effect tunnelling transistors, memory devices, phototransistors, etc.

ACKNOWLEDGMENTS

M. Z. and P. V. acknowledge the support of the Concordia University Grant No. VB0038 and a Concordia University Graduate Fellowship. The work of M. T. was supported by Colorado State University.

Appendix: Relaxation time

The relaxation time is generally a function of the incoming electron's wave vector and at low temperatures only states near the Fermi level will contribute to transport and single-particle properties. Below we provide expressions for the relaxation time at the Fermi energy in the limiting cases $\Delta, \lambda \neq 0, \lambda_R = 0$ and $\Delta, \lambda = 0, \lambda_R \neq 0$, because in these cases the summation over final states can be performed analytically. Within the first Born approximation the

standard formula for the momentum relaxation time has the form

$$\frac{1}{\tau_\zeta} = \frac{1}{\tau_{\xi k}^\eta} = \frac{2\pi n_i}{\hbar} \sum_{\xi', \eta', k'} |\langle \xi, \eta, k | U(\mathbf{r}) | \xi', \eta', k' \rangle|^2 \delta(E_{\xi k} - E_{\xi' k'}) (1 - \cos \theta), \quad (\text{A.1})$$

where $U(\mathbf{r})$ is the impurity potential, n_i the impurity density, and θ the angle between the initial k and final k' wave vectors. Equation (A.1) holds only for elastic scattering ($\xi = \xi', \eta = \eta', k = k'$) and for central potentials $U(\mathbf{r})$ i.e. $U(\mathbf{r}) = U(r)$. The results for two types of impurity potentials are as follows.

Short-range impurities. We have $U(\mathbf{r}) = U_0 \delta(\mathbf{r} - \mathbf{r}_i)$ where \mathbf{r} and \mathbf{r}_i are the position vectors of the electron and impurity, respectively, and U_0 is the strength of potential. In this case $U(\mathbf{q}) = U_0$ is the Fourier transform of $U(\mathbf{r}) = (1/\sqrt{L_x L_y}) \sum_{\mathbf{q}} U(q) e^{i\mathbf{q}\cdot\mathbf{r}}$ with $|\mathbf{q}| = 2k \sin(\theta/2)$. The results are:

i) $\lambda_R = 0$

$$\frac{1}{\tau_{skF}^\eta} = \frac{V_0^2 n_i (N_s^\eta)^4 \sqrt{\Delta^2 + (\hbar v_F k)^2}}{\hbar (\hbar v_F)^2} [(A_s^\eta)^4 - (A_s^\eta)^2 + 1]. \quad (\text{A.2})$$

In the limit $\Delta, \lambda = 0$, the above result reduces to graphene's scattering time Eq. (24) of Ref. [61]

$$\frac{1}{\tau_{kF}} = \frac{V_0^2 n_i k}{4\hbar^2 v_F}. \quad (\text{A.3})$$

Also, for $\lambda = 0$ Eq. (A.2) agrees with the result for topological insulators [58].

ii) $\Delta, \lambda = 0$

$$\frac{1}{\tau_{skF}^\eta} = \frac{V_0^2 n_i (N_s^\eta)^4 \sqrt{\lambda_R^2 + (\hbar v_F k)^2}}{\hbar^3 v_F^2} \left[[(A_s^\eta)^2 + (B_s^\eta)^2]^2 + (C_s^\eta)^4 - [1 + (C_s^\eta)^2][(A_s^\eta)^2 + (B_s^\eta)^2] - 2(C_s^\eta)^2 + 1 \right]. \quad (\text{A.4})$$

Long-range impurities. We assume $U(\mathbf{r}) = eQe^{-k_s r}/4\pi\epsilon_0\epsilon r$, where k_s is the screening wave vector, Q is the charge of the impurity, and ϵ the dielectric constant. In this case $U(q) = 2\pi U_0/\sqrt{k_s^2 + q^2}$ with $U_0 = eQ/4\pi\epsilon_0\epsilon$. The results are:

i) $\lambda_R = 0$

$$\frac{1}{\tau_{skF}^\eta} = \frac{V_0^2 n_i (N_s^\eta)^4 \sqrt{\Delta^2 + (\hbar v_F k)^2}}{2\hbar^3 v_F^2 k^2} \left[[1 + (A_s^\eta)^4] \left[1 - \frac{a_s}{\sqrt{a_s^2 + 1}} \right] + 2(A_s^\eta)^2 \left[2a_s^2 - \frac{a_s(2a_s^2 + 1)}{\sqrt{a_s^2 + 1}} \right] \right]. \quad (\text{A.5})$$

In the limit $\Delta = \lambda = 0$ we set $a_s = k_s/2k$ and obtain the relaxation time in pristine graphene [63]

$$\frac{1}{\tau_{kF}} = \frac{V_0^2 n_i (a_s - \sqrt{a_s^2 + 1})^2}{4\hbar^2 v_F k}. \quad (\text{A.6})$$

Moreover, for $\lambda = 0$ Eq. (A.5) gives the relaxation time for topological insulators [58].

ii) $\Delta, \lambda = 0$

$$\begin{aligned} \frac{1}{\tau_{skF}^\eta} = & \frac{V_0^2 n_i (N_s^\eta)^4 \sqrt{\lambda_R^2 + (\hbar v_F k)^2}}{2\hbar^3 v_F^2 k^2} \left[1 + [(A_s^\eta)^2 + (B_s^\eta)^2]^2 + (C_s^\eta)^4 \left[1 - \frac{a_s}{\sqrt{a_s^2 + 1}} \right] \right. \\ & + 2[1 + (C_s^\eta)^2][(A_s^\eta)^2 + (B_s^\eta)^2] \left[2a_s^2 - \frac{a_s(2a_s^2 + 1)}{\sqrt{a_s^2 + 1}} \right] \\ & \left. - 2(C_s^\eta)^2 \left[1 + \frac{a_s}{\sqrt{a_s^2 + 1}} + 8a_s^3 \sqrt{a_s^2 + 1} - 8a_s^2(2a_s^2 + 1) \right] \right]. \end{aligned} \quad (\text{A.7})$$

- [2] N. Tombros, C. Jozsa, M. Popinciuc, H. T. Jonkman, and B. J. van Wees, *Nature* **448**, 571 (2007).
- [3] J. Ingla-Aynés, M. H. D. Guimarães, R. J. Meijerink, P. J. Zomer, and B. J. van Wees, *Phys. Rev. B* **92**, 201410(R) (2015).
- [4] M. Drögeler, C. Franzen, F. Volmer, T. Pohlmann, L. Banszerus, M. Wolter, K. Watanabe, T. Taniguchi, C. Stampfer, and B. Beschoten, *Nano Lett.* **16**, 3533 (2016).
- [5] C. L. Kane and E. J. Mele, *Phys. Rev. Lett.* **95**, 226801 (2005).
- [6] Z. Qiao, S. A. Yang, W. Feng, W.-K. Tse, J. Ding, Y. Yao, Y. Wang and Q. Niu, *Phys. Rev. B* **82**, 161414 (2010); C.-X. Liu, S.-C. Zhang and X.-L. Qi, *Annu. Rev. Condens. Matter Phys.* **7**, 301 (2016); Y. Ren, Z. Qiao and Q. Niu, *Rep. Prog. Phys.* **79**, 066501 (2016); H. Weng, R. Yu, X. Hu, X. Dai and Z. Fang, *Adv. Phys.* **64**, 227 (2015).
- [7] A. H. C Neto, and F. Guinea, *Phys. Rev. Lett.* **103**, 026804 (2009).
- [8] C. Weeks, J. Hu, J. Alicea, M. Franz and R. Wu, *Phys. Rev. X* **1**, 021001 (2011).
- [9] J. Ding, Z. Qiao, W. Feng, Y. Yao and Q. Niu, *Phys. Rev. B* **84**, 195444 (2011).
- [10] J. Hu, J. Alicea, R. Wu and M. Franz, *Phys. Rev. Lett.* **109**, 266801 (2012).
- [11] D. Ma, Z. Li and Z. Yang, *Carbon* **50**, 297 (2012).
- [12] K.-H. Jin and S.-H. Jhi, *Phys. Rev. B* **87**, 075442 (2013).
- [13] A. Ferreira, T. G. Rappoport, M. A. Cazalilla and A. H. C. Neto, *Phys. Rev. Lett.* **112**, 066601 (2014).
- [14] A. A. Kaverzin and B. J. van Wees, *Phys. Rev. B* **91**, 165412 (2015).
- [15] J. Balakrishnan, G. K. W. Koon, M. Jaiswal, A. H. C. Neto and B. C. Ozyilmaz, *Nat. Phys.* **9**, 284 (2013).
- [16] X. Hong, S.-H. Cheng, C. Herding, and J. Zhu, *Phys. Rev. B* **83**, 085410 (2011).
- [17] Z. Jia, B. Yan, J. Niu, Q. Han, R. Zhu, D. Yu and X. Wu, *Phys. Rev. B* **91**, 085411 (2015).
- [18] U. Chandni, E. A. Henriksen and J. P. Eisenstein, *Phys. Rev. B* **91**, 245402 (2015).
- [19] Y.-C. Lin, N. Lu, N. Perea-Lopez, J. Li, Z. Lin, X. Peng, C. H. Lee, C. Sun, L. Calderin, P. N. Browning, M. S. Bresnehan, M. J. Kim, T. S. Mayer, M. Terrones, and J. A. Robinson, *ACS Nano* **8**, 3715 (2014).
- [20] M.-Y. Lin, C.-E. Chang, C.-H. Wang, C.-F. Su, C. Chen, S.-C. Lee, and S.-Y. Lin, *Appl. Phys. Lett.* **105**, 073501 (2014).
- [21] A. Azizi, S. Eichfeld, G. Geschwind, K. Zhang, B. Jiang, D. Mukherjee, L. Hossain, A. F. Piasecki, B. Kabius, J. A. Robinson, and N. Alem, *ACS Nano* **9**, 4882 (2015).
- [22] Y. Kim, D. Choi, W. J. Woo, J. B. Lee, G. H. Ryu, J. H. Lim, S. Lee, Z. Lee, S. Im, J.-H. Ahn, W.-H. Kim, J. Park, and H. Kim, *Appl. Surf. Sci.* **494**, 591 (2019).
- [23] A. M. Alsharari, M. M. Asmar, and S. E. Ulloa, *Phys. Rev. B* **98**, 195129 (2018).
- [24] L. A. Benitez, J. F. Sierra, W. S. Torres, A. Arrighi, F. Bonnell, M. V. Costache, and S. O. Valenzuela, *Nat. Phys.* **14**, 303 (2018).
- [25] A. W. Cummings, J. H. Garcia, J. Fabian, and S. Roche, *Phys. Rev. Lett.* **119**, 206601 (2017).
- [26] W. Han, R. K. Kawakami, M. Gmitra, and J. Fabian, *Nat. Nanotechnol.* **9**, 794 (2014).
- [27] K. F. Mak, C. Lee, J. Hone, J. Shan, and T. F. Heinz, *Phys. Rev. Lett.* **105**, 136805 (2010).
- [28] A. Kormányos, G. Burkard, M. Gmitra, J. Fabian, V. Zólyomi, N. D. Drummond, and V. Falkó, *2D Mater.* **2**, 022001 (2015).
- [29] C.-P. Lu, G. Li, K. Watanabe, T. Taniguchi, and E. Y. Andrei, *Phys. Rev. Lett.* **113**, 156804 (2014).
- [30] S. Larentis, J. R. Tolsma, B. Fallahzad, D. C. Dillen, K. Kim, A. H. MacDonald, and E. Tutuc, *Nano Lett.* **14**, 2039 (2014).
- [31] L. Banszerus, T. Sohler, A. Epping, F. Winkler, F. Libisch, F. Haupt, K. Watanabe, T. Taniguchi, K. Müller-Caspary, N. Marzari, F. Mauri, B. Beschoten, and C. Stampfer, arXiv: 1909.09523.
- [32] S. Bertolazzi, D. Krasnozhon, and A. Kis, *ACS Nano* **7**, 3246 (2013).
- [33] K. Roy, M. Padmanabhan, S. Goswami, T. P. Sai, G. Ramalingam, S. Raghavan, and A. Ghosh, *Nat. Nanotechnol.* **8**, 826 (2013).
- [34] W. Zhang, C.-P. Chuu, J.-K. Huang, C.-H. Chen, M.-L. Tsai, Y.-H. Chang, C.-T. Liang, Y.-Z. Chen, Y.-L. Chueh, J.-H. He, M.-Y. Chou, and L.-J. Lib, *Sci. Rep.* **4**, 3826 (2014).
- [35] N. A. Kumar, M. A. Dar, R. Gul, and J. Baek, *Mater. Today* **18**, 286 (2015).
- [36] L. Britnell, R. V. Gorbachev, R. Jalil, B. D. Belle, F. Schedin, A. Mishchenko, T. Georgiou, M. I. Katsnelson, L. Eaves, S. V. Morozov, N. M. R. Peres, J. Leist, A. K. Geim, K. S. Novoselov and L. A. Ponomarenko, *Science* **335**, 947 (2012).
- [37] A. Mishchenko, J. S. Tu, Y. Cao, R. V. Gorbachev, J. R. Wallbank, M. T. Greenaway, V. E. Morozov, S. V. Morozov, M. J. Zhu, S. L. Wong, F. Withers, C. R. Woods, Y.-J. Kim, K. Watanabe, T. Taniguchi, E. E. Vdovin, O. Makarovskiy, T. M. Fromhold, V. I. Fal'ko, A. K. Geim, L. Eaves and K. S. Novoselov, *Nat. Nanotechnol.* **9**, 808 (2014).
- [38] K. Roy, M. Padmanabhan, S. Goswami, T. P. Sai, G. Ramalingam, S. Raghavan and A. Ghosh, *Nat. Nanotechnol.* **8**, 826 (2013).
- [39] A. David, P. Rakyta, A. Kormányos, and Guido Burkard, *Phys. Rev. B* **100**, 085412 (2019).
- [40] Y. Li and M. Koshino, *Phys. Rev. B* **99**, 075438 (2019).
- [41] A. Avsar, J. Y. Tan, T. Taychatanapat, J. Balakrishnan, G. K. W. Koon, Y. Yeo, J. Lahiri, A. Carvalho, A. S. Rodin, E. C. T. O'Farrell, G. Eda, A. H. C. Neto and B. Özyilmaz, *Nat. Commun.* **5**, 4875 (2014).
- [42] M. Gmitra, S. Konschuh, C. Ertler, C. Ambrosch-Draxl, and J. Fabian, *Phys. Rev. B* **80**, 235431 (2009).
- [43] C. K. Safeer, J. Ingla-Aynés, F. Herling, J. H. Garcia, M. Vila, N. Ontoso, M. Reyes Calvo, S. Roche, L. E. Hueso, and F. Casanova, *Nano Lett.* **19**, 1074 (2019).
- [44] B. Yang, M.-F. Tu, J. Kim, Y. Wu, H. Wang, J. Alicea, R. Wu, M. Bockrath and J. Shi, *2D Mater.* **3**, 031012 (2016).
- [45] S. Zihlmann, A. W. Cummings, J. H. Garcia, M. Kedves, K. Watanabe, T. Taniguchi, C. Schonenberger, and P. Makk, *Phys. Rev. B* **97**, 075434(R) (2018).
- [46] Z. Wang, D. K. Ki, H. Chen, H. Berger, A. H. MacDonald, and A. F. Morpurgo, *Nat. Commun.* **6**, 8339 (2015).
- [47] Jose H. Garcia, Marc Vila, Aron W. Cummings, and Stephan Roche, *Chem. Soc. Rev.* **47**, 3359 (2018); A. Mreńca-Kolasinińska, B. Rzeszutarski, and B. Szafran, *Phys. Rev. B* **98**, 045406 (2018).
- [48] T. Völkl, T. Rockinger, M. Drienovsky, K. Watanabe, T. Taniguchi, D. Weiss, and J. Eroms, *Phys. Rev. B* **96**, 125405 (2017); B. Yang, E. Molina, J. Kim, D. Bar-

- roso, M. Lohmann, Y. Liu, Y. Xu, R. Wu, L. Bartels, K. Watanabe, T. Taniguchi, and Jing Shi, *Nano Lett.* **18**, 3580 (2018).
- [49] M. Gmitra, D. Kochan, P. Högl, and J. Fabian, *Phys. Rev. B* **93**, 155104 (2016).
- [50] M. Gmitra and J. Fabian, *Phys. Rev. B* **92**, 155403 (2015).
- [51] M. Gmitra, D. Kochan, and J. Fabian, *Phys. Rev. Lett.* **110**, 246602 (2013).
- [52] Z. Wang, D.-K. Ki, J. Y. Khoo, D. Mauro, H. Berger, L. S. Levitov, and A. F. Morpurgo, *Phys. Rev. X* **6**, 041020 (2016).
- [53] M. Charbonneau, K. M. Van Vliet, and P. Vasilopoulos, *J. Math. Phys.* **23**, 318 (1982).
- [54] D. Xiao, W. Yao, and Q. Niu, *Phys. Rev. Lett.* **99**, 236809 (2007).
- [55] A. Rycerz, J. Tworzydło, and C. W. J. Beenakker, *Nat. Phys.* **3**, 172 (2007).
- [56] Z. Li and J. P. Carbotte, *Phys. Rev. B* **86**, 205425 (2012).
- [57] V. P. Gusynin, S. G. Sharapov, and J. P. Carbotte, *Phys. Rev. Lett.* **96**, 256802 (2006).
- [58] V. Vargiamidis and P. Vasilopoulos, *J. Appl. Phys.* **116**, 063713 (2014).
- [59] D. S. L. Abergel and V. I. Fal'ko, *Phys. Rev. B* **75**, 155430 (2007).
- [60] E. J. Nicol and J. P. Carbotte, *Phys. Rev. B* **77**, 155409 (2008).
- [61] T. Stauber, N. M. R. Peres, and F. Guinea, *Phys. Rev. B* **76**, 205423 (2007).
- [62] K. Nomura and A. H. MacDonald, *Phys. Rev. Lett.* **98**, 076602 (2007).
- [63] A. A. Patel and S. Mukerjee, *Phys. Rev. B* **86**, 075411 (2012).